Distinct classes of lamina-associated domains are defined by differential patterns of repressive histone methylation

Caden J. Martin, Elizabeth A. Oser, Prabakaran Nagarajan, et al.

Genome Res. 2025 35: 1959-1974 originally published online August 5, 2025
Access the most recent version at doi:10.1101/gr.280380.124

Research

Distinct classes of lamina-associated domains are defined by differential patterns of repressive histone methylation

Caden J. Martin,[1] Elizabeth A. Oser,[1] Prabakaran Nagarajan,[1] Liudmila V. Popova,[1] Benjamin D. Sunkel,[2] Benjamin Z. Stanton,[2] and Mark R. Parthun[1]

[1]*Department of Biological Chemistry and Pharmacology, The Ohio State University, Columbus, Ohio 43210, USA;* [2]*Abigail Wexner Research Institute at Nationwide Children's Hospital, Columbus, Ohio 43205, USA*

A large fraction of the genome interacts with the nuclear periphery through lamina-associated domains (LADs), repressive regions which play an important role in genome organization and gene regulation across development. Despite much work, LAD structure and regulation are not fully understood, and a mounting number of studies have identified numerous genetic and epigenetic differences within LADs, demonstrating they are not a uniform group. Here, we profile lamin B1, CBX1 (also known as HP1B), H3K9me3, H3K9me2, H3K27me3, H3K14ac, H3K27ac, and H3K9ac in MEF cell lines derived from the same mouse colony, and cluster LADs based on the abundance and distribution of these features across LADs. We find that LADs fall into three groups, each enriched in a unique set of histone modifications and genomic features. Each group is defined by a different heterochromatin modification (H3K9me3, H3K9me2, or H3K27me3), suggesting that all three of these marks play important roles in regulation of LAD chromatin and potentially of lamina association. We also discover unique features of LAD borders, including a LAD border–specific enrichment of H3K14ac. These results reveal important distinctions between LADs and highlight the rich diversity and complexity in LAD structure and regulatory mechanisms.

[Supplemental material is available for this article.]

Histone posttranslational modifications (PTMs) help shape the three-dimensional organization of the genome. They distinguish different states of chromatin, mediate transcriptional activation and repression, and regulate the physical properties of chromatin (Janssen and Lorincz 2022; Macrae et al. 2023). They also play a crucial role in transmitting the memory of chromatin state and cell identity through cell division (Escobar et al. 2021).

Most actively transcribed genes are found in euchromatin, which is relatively decondensed, enriched in histone acetylation, transcription factor binding, and RNA polymerase II, and largely localizes to the nuclear interior. Heterochromatin is transcriptionally repressive and highly compacted. It comes in two distinct forms, which contribute to gene repression through different mechanisms. Facultative heterochromatin tends to silence genes in a developmental or cell type–specific manner (Kim and Kingston 2022). It is depleted in histone acetylation and is distinguished by enrichment of H3K27 trimethylation (H3K27me3). Constitutive heterochromatin is enriched in features like H3K9 di- and trimethylation (H3K9me2/3) and the H3K9me2/3-binding protein CBX1 (also known as HP1B). It is likewise depleted in histone acetylation and generally localizes to the nuclear periphery or chromocenters (Allshire and Madhani 2018; Grewal 2023). Constitutive heterochromatin is traditionally defined as domains of heterochromatin which remain silenced across different cell types and block transcription of constitutively silent regions like centromeres, telomeres, and repetitive elements. However, regions with features characteristic of constitutive heterochromatin can also function in cell type–specific gene regulation (Nicetto and Zaret 2019; Nicetto et al. 2019; Padeken et al. 2022). In addition to its role in transcriptional repression, constitutive heterochromatin helps regulate genome architecture and stability (van Steensel and Belmont 2017; Falk et al. 2019).

Lamina-associated domains (LADs) are large, heterochromatic regions of the genome that interact with the transcriptionally repressive environment of the nuclear lamina. Some LADs are conserved across development, whereas others interact with the lamina only in particular cell types, leading to the subdivision of LADs into constitutive LADs (cLADs) and facultative LADs (fLADs) (not to be confused with constitutive and facultative heterochromatin) (Peric-Hupkes et al. 2010; Shah et al. 2023). Constitutive LADs are found associated with the nuclear lamina across nearly all cell types examined to date, whereas the lamina association of facultative LADs varies across cell types. These are not inflexible categories, however, as cell types can be found with unusual patterns of lamina association or no association at all (Solovei et al. 2009; Borsos et al. 2019).

Multiple mechanisms mediate the physical interaction of LADs with the nuclear periphery (Zullo et al. 2012; Bian et al. 2013; Manzo et al. 2022). LADs are classically characterized by marks of constitutive heterochromatin. H3K9m2 and H3K9me3 are both enriched in LADs and can promote localization of chromatin to the periphery (Peric-Hupkes et al. 2010; Bian et al. 2013; Kind et al. 2013; Poleshko et al. 2017, 2019; Smith et al. 2021a; Keenan et al. 2024). CBX1, an important mediator of gene silencing and gene compaction, binds H3K9me2/3 and helps link chromatin to the periphery through interactions with A- and

Corresponding author: Parthun.1@osu.edu
Article published online before print. Article, supplemental material, and publication date are at https://www.genome.org/cgi/doi/10.1101/gr.280380.124. Freely available online through the *Genome Research* Open Access option.

B-type lamins and lamin-associated proteins such as LBR and PRR14 (Ye and Worman 1996; Poleshko et al. 2013). LBR has been found to interact with histones bearing both H3K9me2 and H3K9me3, as well as with at least one of the heterochromatin protein 1 isoforms (CBX1/3/5) (Ye and Worman 1996; Bannister et al. 2001; Makatsori et al. 2004; Lechner et al. 2005). Other peripheral proteins such as LEM (LAP2-EMERIN-MAN1) domain-containing proteins can also contribute to chromatin tethering (Briand and Collas 2020; Alagna et al. 2023).

Some evidence has supported a role for the facultative mark H3K27me3 in regulating the association of LADs with the nuclear lamina, but this is not well characterized (Harr et al. 2015; Guerreiro and Kind 2019; Siegenfeld et al. 2022). H3K27me3 is specifically enriched at LAD borders and some smaller, more gene-rich LADs (Guelen et al. 2008; Sadaie et al. 2013; Harr et al. 2015; Tran et al. 2021; Alagna et al. 2023; Gholamalamdari et al. 2025). H3K27me3 peaks at LAD borders are believed to insulate the constitutive heterochromatin inside LADs from euchromatin outside of the LAD (Guelen et al. 2008; Siegenfeld et al. 2022).

Multiple factors complicate understanding of LAD structure and regulation. One is the large degree of redundancy between tethering mechanisms and the diversity in peripheral proteins which can interact with chromatin, many of which are differentially expressed between different tissues and stages of development. Added to this is the variability of LADs themselves. Whereas they are consistently heterochromatic and generally transcriptionally repressive, LADs show mixed abilities to silence genes and gene reporters, which is often dependent on the chromatin context and the promoter itself (Leemans et al. 2019; Alagna et al. 2023). Previous studies have uncovered a lack of uniformity across LADs in their MNase accessibility, linker histone enrichment, lamin B1 occupancy, CTCF dependency, primary lamin interactor (B or A/C), histone PTM enrichment, and more (Bian et al. 2013; Lund et al. 2015; Zheng et al. 2015; Vertii et al. 2019; Kaczmarczyk et al. 2022; Alagna et al. 2023; Shah et al. 2023; Gholamalamdari et al. 2025). Although some degree of variation across the genome is expected for any set of genomic features, these studies suggest that LADs cannot be simply characterized as a single group and may fall into subcategories with distinct structures, functions, and modes of regulation.

We hypothesized that much of this diversity among LADs was reflected in and potentially driven by unique signatures of histone PTMs which could give rise to LAD subclasses with different modes of regulation. Thus, we determined to test whether the levels of histone PTMs, lamin B1 association, and the important heterochromatin regulator CBX1 could be used to classify LADs into structurally and functionally distinct categories.

Results

Comparison of LADs derived from a single set of related cell lines

To understand the structure and regulation of lamina-associated chromatin, we determined the genome-wide localization of lamin B1 (CUT&RUN), CBX1 (ChIP-seq), and six different histone modifications (CUT&Tag) in immortalized mouse embryonic fibroblast (iMEF) cell lines derived from a single colony of wild-type C57BL6/J mice. We identified LADs in our iMEFs by performing CUT&RUN for lamin B1 and called them using a modified version of the HMMt package in R with parameters optimized for our data (see Methods for details). To validate our LAD set, we compared it with previously published maps of LADs created in NIH3T3 MEFs using LaminB1-DamID (Peric-Hupkes et al. 2010; Meuleman et al. 2013). We also compared with a LAD map generated in NIH3T3 MEFs using lamin B1 CUT&RUN (referred to by those authors as GO-CaRT rather than CUT&RUN) (Fig. 1A; Ahanger et al. 2021). Chromosomes X and Y were excluded from this and all subsequent analyses due to suboptimal lamin B1 mapping on the sex chromosomes. DamID indicated that LADs comprise 41.5% of the genome of NIH3T3 cells, and GO-CaRT came to a similar figure of 38.4%, whereas CUT&RUN in C57BL6/J iMEFs indicated that LADs cover 47.8% of the genome (Fig. 1A). DamID and GO-CaRT LADs show 88% and 92% overlap, respectively, with chromatin identified as lamina-associated by CUT&RUN. The overlap between LADs detected by DamID, GO-CaRT, and CUT&RUN is illustrated by tracks of the $\log_2$ fold enrichment of lamin B1 determined by each method (Fig. 1B). The differences between LAD sets can be broadly attributed to either biological or technical factors. The lower right inset of Figure 1B illustrates a technical difference where our LAD calling was more successful than the DamID data set. Clear lamin B1 signal can be seen across a large domain, which is identified by our algorithm and the GO-CaRT analysis but only partially identified by the algorithm used to analyze the DamID data. The lower left inset shows a difference that likely arose from biological factors, as the LAD is called in NIH3T3 cells by DamID and GoCaRT but not in our MEFs, which display much weaker lamin B1 signal. The center inset of Figure 1B illustrates another difference arising from biological factors. The LAD detected in C57BL6/J iMEFs is significantly larger due to clear detection of lamin B1 interaction that is not seen in the NIH3T3 MEFs by either DamID or GO-CaRT. Figure 1A suggests that technical and biological factors both contribute to the differences between our LAD set and those published previously. However, biological variation appears to account for more differences, as there is more variation between our LAD set and the GO-CaRT LAD set, which were generated by the same method in different cell lines, than between the GO-CaRT LAD set and the DamID LAD set, which were generated by different methods in the same cell line. For all subsequent analyses, we use the LAD definitions determined by CUT&RUN in our C57BL6/J iMEFs. If we repeat these analyses using the previous LAD set from NIH3T3 cells, we obtain largely similar results (Supplemental Fig. S1A,B).

Visual inspection of the genome browser suggests that not all LADs have equal levels of lamin B1 signal. To see if the abundance of lamin B1 signal corresponds at least partially to facultative and constitutive LADs, we compared the signal between the two groups but did not see a notable difference (Supplemental Fig. S1C). However, dividing LADs into those called only in our MEFs versus those called both in our iMEFs and by DamID in NIH3T3 cells did show a small but significant difference. This suggests that LADs unique to our MEFs have slightly lower levels of lamin B1 association than shared LADs and may be slightly more variable across the cell population (Supplemental Fig. S1D).

LAD borders show enrichment of multiple histone modifications

To determine the structure of chromatin across LADs, we used CUT&Tag to map a variety of histone PTMs, including the euchromatin marks H3K9ac, H3K14ac, and H3K27ac, facultative heterochromatin mark H3K27me3, and constitutive heterochromatin marks H3K9me2 and H3K9me3. We also used ChIP-seq to profile the H3K9 methylation binding protein CBX1.

Scaling all LADs to a uniform size, we plotted the abundance of each feature across the LAD body and around the LAD border

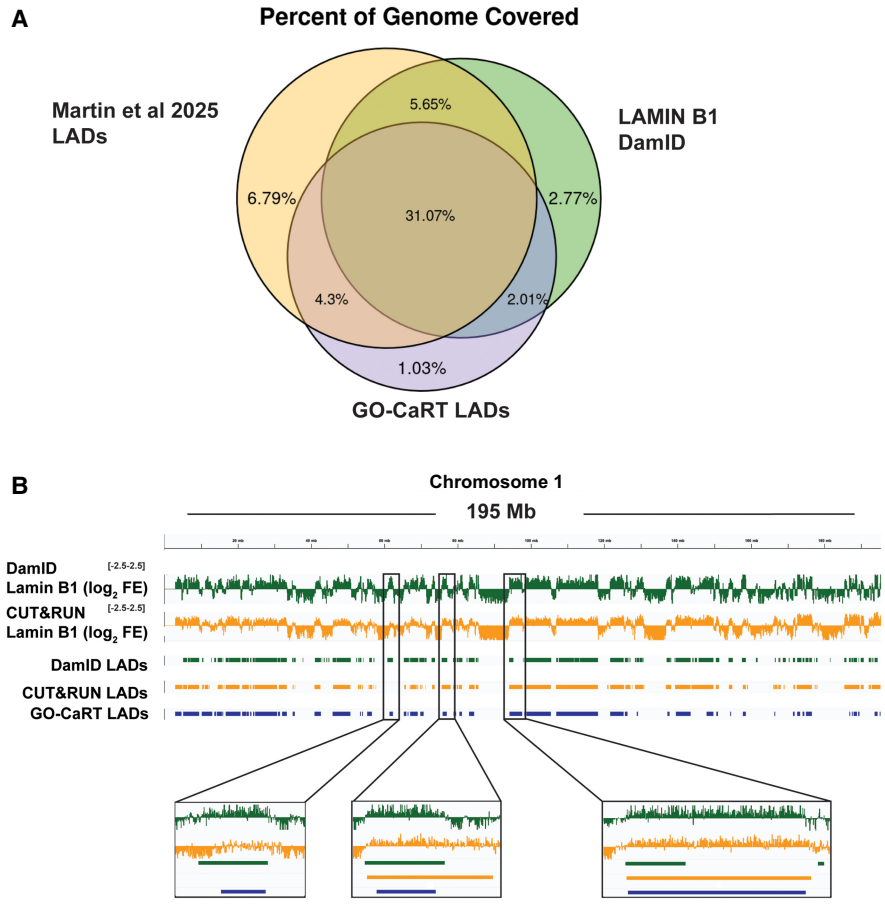

Figure 1. Mapping chromatin–lamin B1 interactions in MEFs using CUT&RUN. (*A*) Fraction of base pairs in the genome covered by our CUT&RUN-generated LAD map (yellow), a DamID-generated LAD map in NIH3T3 cells (green), or a CUT&RUN-generated LAD map in NIH3T3 cells (blue). (*B*) Lamin B1 $\log_2$ fold-enrichment over IgG illustrating differences between our CUT&RUN-generated LAD map in and published maps generated by DamID or CUT&RUN in NIH3T3 cells. *Left inset* shows an example of a LAD called in the DamID data set but not ours. *Middle inset* shows a LAD called differently between the two data sets for biological or experimental reasons. *Right inset* shows a LAD called in our data set but only partially in the DamID data set.

(Fig. 2A,B). As expected, we saw broad domains of CBX1, lamin B1, and the constitutive heterochromatin mark H3K9me3 across LAD interiors. We observed a different pattern for the other constitutive heterochromatin mark, H3K9me2. H3K9me2 is present as a peak just inside of LAD borders and decreases to an intermediate level across the interior of LADs. The facultative heterochromatin mark H3K27me3 was also present as a sharp peak right at LAD borders that then sharply decreased across the LAD interiors to levels at or below the surrounding chromatin, as previously described (Guelen et al. 2008; Sadaie et al. 2013; Harr et al. 2015).

H3K9ac and H3K27ac were essentially depleted throughout the interior of LADs then abruptly increased outside LAD borders (Fig. 2B,C). In contrast, H3K14ac formed a broad peak inside of the LAD border which gradually decreased across the interior of the LAD (Fig. 2B,C). The presence of significant levels of H3K14ac throughout the interior of LADs indicates that these regions can be permissive to acetylation at certain sites. The locations of the H3K14ac and H3K27me3 peaks did not coincide at LAD borders. H3K27me3 reaches its maximum level exactly at the LAD border, whereas H3K14ac reaches its maximum a few kilobases to tens of kilobases inside the LAD.

To confirm that this unanticipated enrichment of H3K9me2 at LAD borders was not an artifact of the technique or antibody used, we used CUT&RUN to profile H3K9me2 using the same antibody and using an alternative antibody. We included EpiCypher's K-MetStat Panel of barcoded posttranslationally modified nucleosomes to verify antibody specificity for H3K9me2. Results from the K-MetStat panel showed that our H3K9me2 antibody was indeed specific for H3K9me2 (Supplemental Fig. S2A), and CUT&RUN data showed highly similar distributions between the two different antibodies and between CUT&RUN and CUT&Tag (Supplemental Fig. S2B). Similarly, we profiled H3K14ac using CUT&RUN with an alternative antibody and determined that the genomic distribution of H3K14ac was unchanged between CUT&Tag data generated with the original antibody and CUT&RUN data generated by the second antibody (Supplemental Fig. S2C).

LADs cluster into distinct subtypes

Although LADs are consistently heterochromatic and contribute to gene silencing, prior studies have found variation among LADs in both their physical and chemical properties (Lund et al. 2015; Zheng et al. 2015; Kaczmarczyk et al. 2022; Alagna et al. 2023; Shah et al. 2023; Gholamalamdari et al. 2025). We hypothesized that the chromatin profiles created across all LADs in aggregate (Fig. 2) mask nuance in the chromatin profiles of individual LADs or groups of LADs. To address this, we clustered LADs by scaling them all to a uniform size and dividing the chromatin signal into 24 bins across each LAD, then performing *k*-means clustering on the resulting matrix. A plot of silhouette scores suggested two or three clusters to be optimal, with a slight bias toward two (Fig. 3A). However, we found that dividing into two clusters led to lumping together of LADs which had quite different patterns of modifications. For example, LADs with high H3K9me2/low H3K27me3 and LADs with low H3K9me2/high H3K27me3 were both placed in the same cluster (for examples of such LADs, see Fig. 3D). Thus, we chose to proceed with three clusters. Plotting the first two principle components showed that three clusters could be easily distinguished (Fig. 3B). These contained 392, 518, and 218 LADs, respectively. Notably, performing hierarchical clustering and cutting at three clusters yielded similar clusters to the *k*-means algorithm, although with a reduction in the size of Cluster 3 (Supplemental Fig. S3).

Chromatin profiles across LADs in each cluster revealed stark differences in both the overall abundance of histone PTMs and their pattern over the LAD (Fig. 3C,D). As expected, H3K9ac and H3K27ac are highly depleted across the lengths of all three LAD clusters. Lamin B1 signal was strongly enriched in all clusters, although the degree of enrichment varied slightly. Cluster 1 LADs

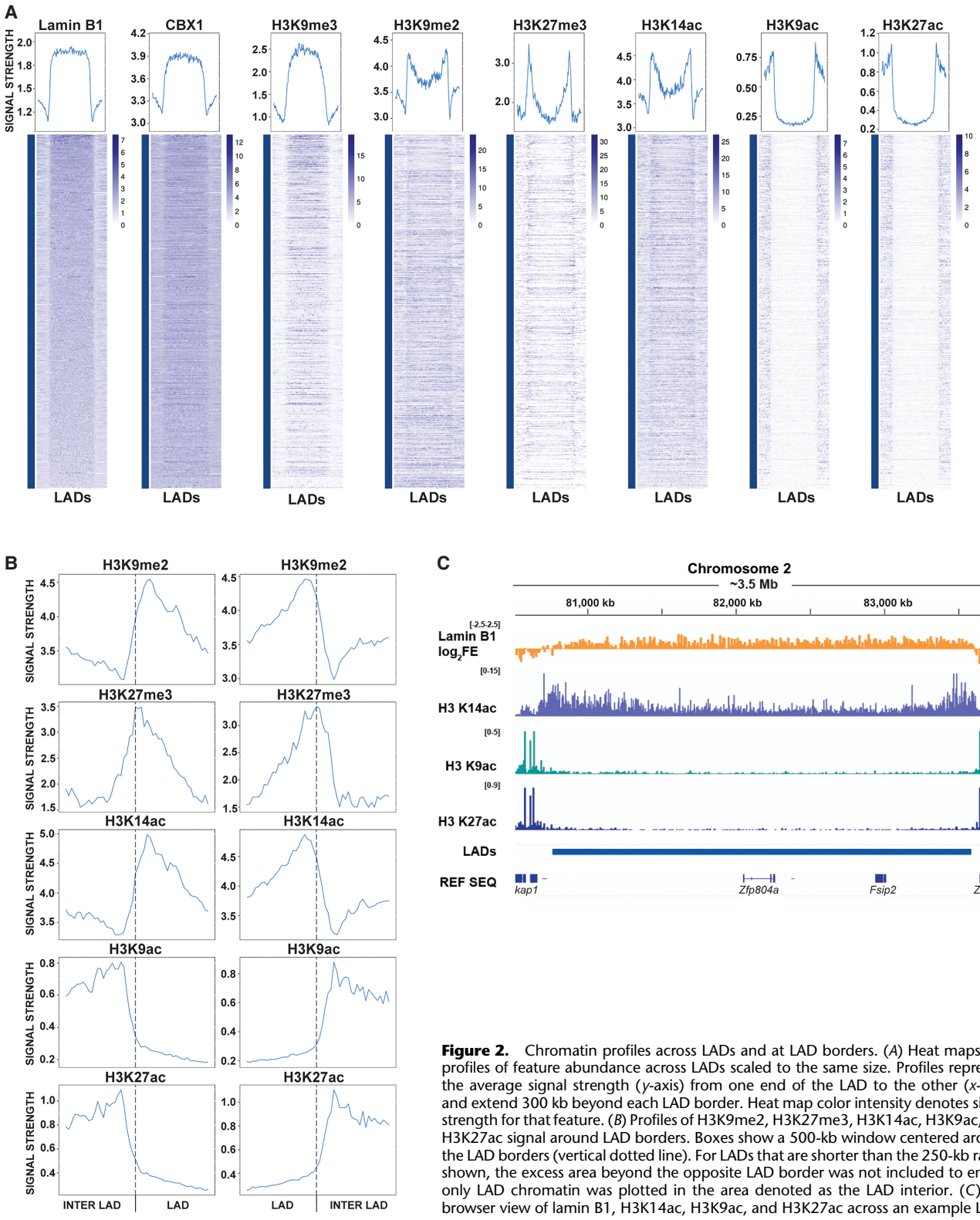

Figure 2. Chromatin profiles across LADs and at LAD borders. (*A*) Heat maps and profiles of feature abundance across LADs scaled to the same size. Profiles represent the average signal strength (*y*-axis) from one end of the LAD to the other (*x*-axis) and extend 300 kb beyond each LAD border. Heat map color intensity denotes signal strength for that feature. (*B*) Profiles of H3K9me2, H3K27me3, H3K14ac, H3K9ac, and H3K27ac signal around LAD borders. Boxes show a 500-kb window centered around the LAD borders (vertical dotted line). For LADs that are shorter than the 250-kb range shown, the excess area beyond the opposite LAD border was not included to ensure only LAD chromatin was plotted in the area denoted as the LAD interior. (*C*) IGV browser view of lamin B1, H3K14ac, H3K9ac, and H3K27ac across an example LAD.

most closely resemble the canonical definition of constitutive heterochromatin in LADs and the structure of LADs observed in aggregate, featuring a broad domain enriched in CBX1 and H3K9me3 across the entire LAD. H3K9me2, H3K27me3, and H3K14ac were depleted throughout the interior of Cluster 1 LADs and then peaked near the LAD border with H3K27me3 at the end of the LADs and H3K9me2 and H3K14ac peaking internal to the peak of H3K27me3.

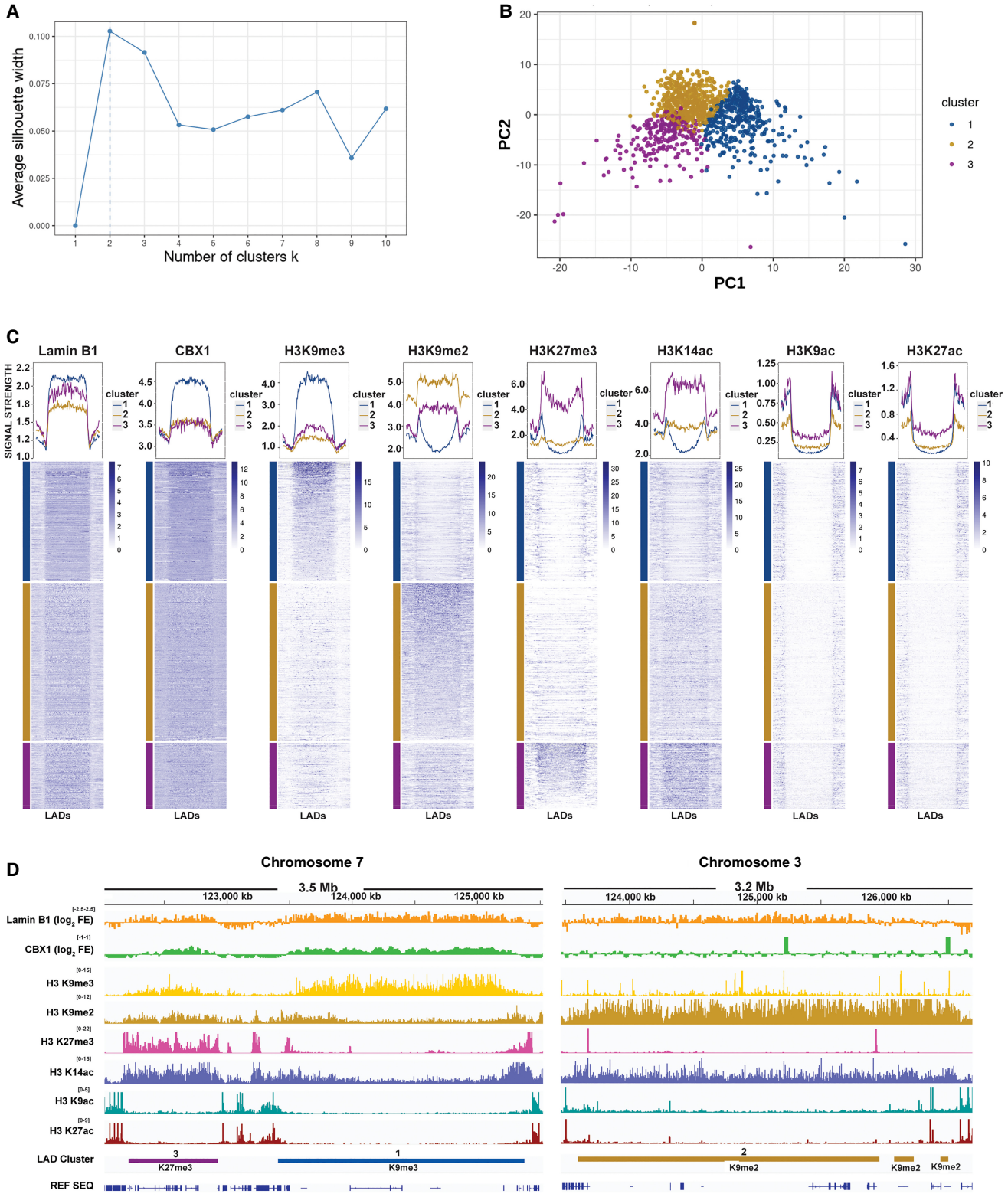

Figure 3. Clustering LADs by chromatin profile. (*A*) Silhouette plot of *k*-means clustering of LADs. (*B*) Principle component plot of LAD clusters. The gold dot at the top of the plot consists of ~two dozen LADs and is the reason the elbow plot suggests four clusters rather than three. (*C*) Heat maps and profiles of feature abundance across LADs, separated into Cluster 1 (blue), Cluster 2 (gold), and Cluster 3 (purple). Profiles represent the average signal strength (*y*-axis) from one end of the LAD to the other (*x*-axis) and extend 300 kb beyond each LAD border. Heat map color intensity denotes signal strength for that feature. (*D*) IGV browser view illustrating examples from each LAD cluster (from *left* to *right*): Cluster 3 (K27me3 LADs) in purple, Cluster 1 (K9me3 LADs) in blue, Cluster 2 (K9me2 LADs) in gold.

Cluster 2 LADs are distinguished by high levels of H3K9me2 across the entire LAD without the prominent peak at the LAD borders observed in Cluster 1 (Fig. 3C,D). They contain only background levels of H3K9me3, low levels of CBX1, and very low levels of H3K27me3 in the LAD interior, with smaller peaks at the borders. H3K14ac is moderately enriched in Cluster 2 LADs at a consistent level that is slightly higher than that observed in euchromatic domains. Similar to H3K27me3, the peak of H3K14ac at Cluster 2 borders is less distinct than in Cluster 1.

Cluster 3 LADs are distinguished by high levels of H3K27me3 across the interior of the LADs with higher levels at the LAD borders (Fig. 3C,D). They are enriched in H3K14ac, which is present across the LAD at levels significantly higher than seen in most regions of euchromatin. H3K9me2 is present at moderate levels and evenly distributed across the LADs with no discernable peak at the borders. Cluster 3 LADs display moderate levels of both H3K9me3 and CBX1.

Each cluster was characterized by enrichment of a different heterochromatin mark: H3K9me3 for Cluster 1, H3K9me2 for Cluster 2, and H3K27me3 for Cluster 3. To learn which marks contribute most to the differences between clusters, we trained a random forest algorithm on our clustering data and looked at which columns were most significant in informing the algorithm's categorization in the resulting decision tree (Supplemental Fig. S4A). Consistent with our observations, many of the columns contributing most to the differences between clusters belong to H3K9me2, H3K9me3, and H3K27me3, with H3K9me2 being particularly significant. H3K14ac also contributes significantly. For all marks, the bins driving the differences between clusters were found in the LAD interior (as opposed to the inner or outer border of the LAD), implying that the LAD interior is where clusters differ most. Further supporting the preeminence of H3K9me2, H3K9me3, and H3K27me3 in defining LAD groups, we found that clustering based on only those three marks yields quite similar groups, with 929/1128 LADs (82.4%) being assigned to the same clusters even with the reduced set of PTMs (Supplemental Fig. S4B,C). Given their distinguishing methylation enrichments, we chose to refer to clusters 1, 2, and 3 as K9me3 LADs, K9me2 LADs, and K27me3 LADs, respectively.

LAD clusters show differing strength of lamina association

We hypothesized that the different patterns of PTM enrichment between the three LAD clusters could affect their three-dimensional organization within the nucleus. We performed 3D DNA FISH to test whether the association with the nuclear lamina varies between clusters, using Lamin A/C staining to visualize the nuclear periphery (Fig. 4; Supplemental Movie S1). Three to four LADs were chosen from each cluster and targeted with DNA FISH probes labeled with a different colored fluorophore for each cluster (Supplemental Table 1). As expected, most LADs from all three clusters were found near or at the nuclear lamina. However, K9me3 and K9me2 LADs showed a statistically significant trend toward closer peripheral localization relative to K27me3 LADs. This highlights the biological significance of these clusters and suggests that different regulatory mechanisms mediate chromatin–lamina interactions in each cluster.

LAD clusters are enriched for different genomic features

Examination of the three LAD clusters shows many differences beyond their histone PTM profiles. K9me3 LADs have a median size of 1.53 Mb, significantly larger than K9me2 LADs and K27me3 LADs, which have median sizes of 0.31 and 0.22 Mb, respectively (Fig. 5A). As a result, K9me3 LADs collectively contain the most genes. However, gene density is highest in K27me3 LADs (Fig. 5B). RNA-seq reveals that differences in gene expression levels between clusters are quite small, but we do observe a higher median expression level in K27me3 LADs compared to the other groups (Fig. 5C). The three LAD clusters also differ in repeat enrichment. K9me3 LADs and K9me2 LADs are highly enriched in LINEs, whereas K27me3 LADs are enriched in SINEs. LTR enrichment is similar across all groups (Fig. 5D).

There is a great difference in the distribution of cLADs and fLADs between the clusters. Constitutive LADs predominate among K9me3 LADs and K9me2 LADs, whereas the majority of K27me3 LADs are facultative (Fig. 5E). This distribution of constitutive and facultative LADs is consistent with the well-characterized involvement of Polycomb silencing in the regulation of developmentally regulated genes (Atlasi and Stunnenberg 2017; Jiang et al. 2024).

We analyzed Gene Ontology and tissue-specific enrichment of genes in each cluster and found numerous terms associated with each cluster. K9me3 LADs were enriched in immune, neuronal, and RNA processing–associated terms (Supplemental Fig. S5). K9me2 LADs were enriched in similar terms, with a particularly strong emphasis on RNA processing. K27me3 LADs were enriched in many terms related to differentiation and cell signaling, suggesting that they contribute to quite different processes. Further, we found a much higher fraction of tissue-specific genes in K27me3 and K9me2 LADs than in K9me3 LADs, consistent with the strongly constitutive heterochromatin character of the latter.

LADs are typically associated with late-replicating regions of chromatin, although differences in replication timing between LADs have been observed (van Schaik et al. 2020; Gholamalamdari et al. 2025). Using publicly available Repli-seq data in MEFs (Rivera-Mulia et al. 2018), we calculated the $\log_2$ ratio of early S-phase to late S-phase replication signal and plotted the distribution between clusters. Whereas all three clusters did indeed favor late replication, there were clear differences between clusters. K27me3 LADs, in particular, showed a tendency towards earlier replication, whereas K9me3 LADs most heavily favored late replication (Fig. 5F).

ChromHMM confirms unique enrichment of states between clusters

To further understand the differences observed between LAD clusters, we ran ChromHMM with our histone modification, CBX1, and lamin B1 data sets. ChromHMM uses a hidden Markov model to identify underlying chromatin states based on the presence or absence of features of interest (e.g., histone PTMs) across the genome. We ran the model using 10-kb bins and found eight states to be optimal for capturing a diversity of chromatin states while avoiding redundancy. The resulting states span the range of active and repressive chromatin, with higher states (e.g., 8) more enriched in euchromatic features like acetylation, and lower states (e.g., 2, 3) showing the most heterochromatic character (Fig. 6A). State 1 is generally depleted in histone marks and appears in various regions across the genome. Unlike H3K9ac and H3K27ac, H3K14ac was not primarily found in the euchromatic state 8 but in heterochromatin states in association with H3K27me3 and H3K9me2.

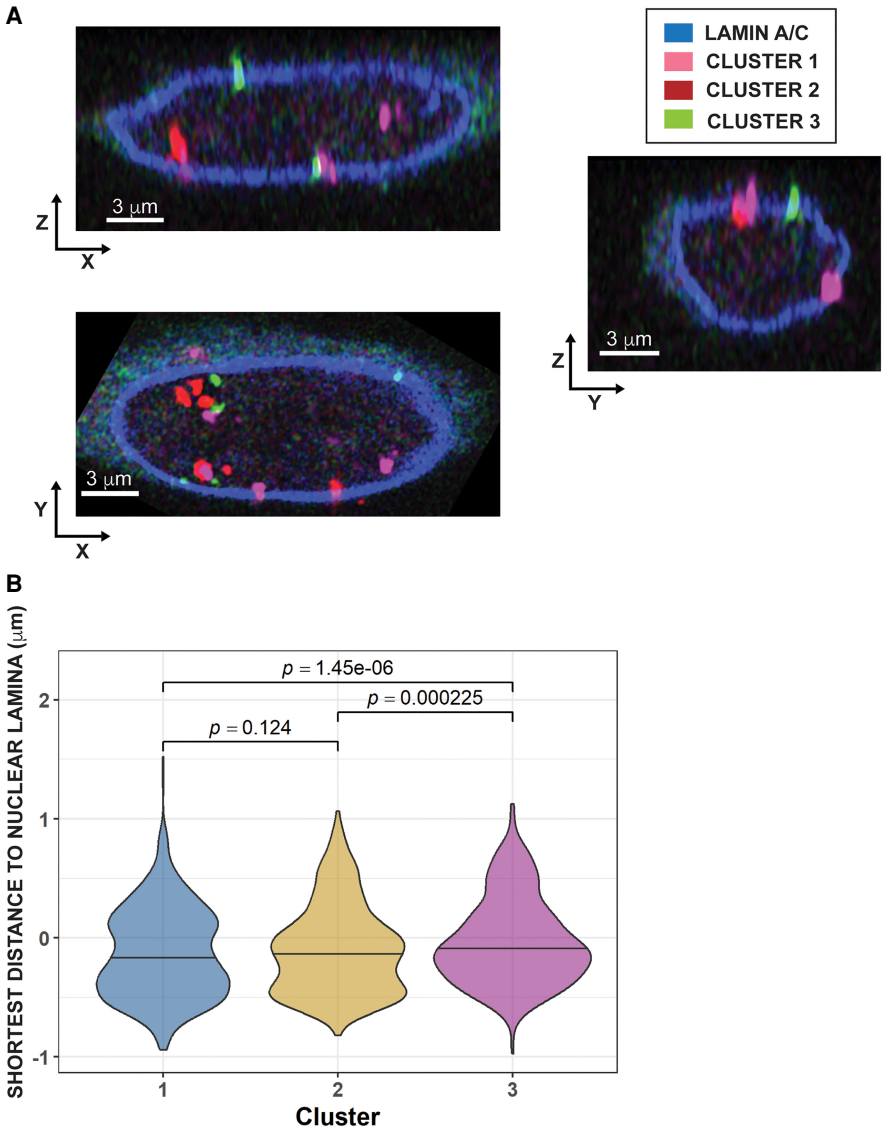

Figure 4. Analysis of cluster localization by DNA FISH. (*A*) Two-dimensional slices showing cluster localization in a representative cell. Individual images capture a subset of the labeled loci present in each cell. (*B*) Violin plot showing distance of representative cluster LADs from the nuclear lamina, as determined by lamin A/C staining (blue). FISH probes were made to target three LADs each from Clusters 1 (pink) and 3 (green) and four LADs from Cluster 2 (red). A total of 58 cells were sampled (see Methods for details).

To compare our observations on the structure of LADs with the states output by ChromHMM, we examined the enrichment of states in each LAD cluster (Fig. 6B,C). As expected, states enriched in K9me3 LADs preferentially contained H3K9me3, the most abundant being states 3 and 4. Also consistent with expectations, the H3K9me2-enriched state 6 predominated in K9me2 LADs, and the H3K27me3-enriched state 7 was the most abundant in K27me3 LADs. Inter-LAD regions were largely enriched in the euchromatic state 8, the variable state 1, and states 5–7 marking non-lamina-associated heterochromatin.

LAD clusters contain distinct states at their borders

Examination of states at LAD borders confirms differences in the border structure of different LAD clusters (Fig. 7). Moving from outside a LAD across the border into a LAD, K9me3 LADs display a clear transition from state 8 to more "LAD Border" states enriched in H3K27me3/H3K14ac, to constitutive heterochromatin inside the LAD (Fig. 7A,B). This transition is altered in K9me2 LADs and K27me3 LADs, which retain high levels of H3K9me2 and H3K27me3, respectively, across both the LAD interior and borders (Fig. 7C,D).

It is possible that the apparent plateau of H3K14ac, H3K27me3, and H3K9me2 across K9me2 LADs and K27me3 LADs is a result of their small size, which does not provide them enough space to decrease into the LAD interior as seen in K9me3 LADs. We examined this by plotting profiles and heat maps of LADs filtered by size (Supplemental Fig. S6). LADs smaller than 250 kb show the expected plateaus for K9me2 LADs and K27me3 LADs. Because there are few K9me3 LADs of this size, their profile is very noisy, but they appear to show a border enrichment for H3K27me3 but not H3K9me2 or H3K14ac. For LADs larger than 1 Mb, K9me2 and K27me3 LADs continue to show plateaus for H3K14ac and H3K9me2, although a slight border enrichment is seen for K9me2 LADs and a clear border enrichment of H3K27me3 is seen for both groups. Thus, LAD size may partially explain the enrichment of H3K27me3 across LAD interiors in K9me2 LADs and K27me3 LADs but poorly accounts for the interior enrichment of H3K9me2 and H3K14ac.

Regression analysis suggests CBX1-independent tethering mechanisms and differences in cluster regulation

Many mechanisms contribute to the localization of chromatin to the nuclear periphery (van Steensel and Belmont 2017; Manzo et al. 2022). Most involve interactions of peripheral proteins with H3K9me2/3, often mediated by CBX1 or its isoform CBX5, which can bind lamina-associated factors such as LBR and PRR14 (Ye and Worman 1996; Ye et al. 1997; Poleshko et al. 2013; Kiseleva et al. 2023). To better understand the factors responsible for mediating chromatin–lamina interactions in C57BL6/J MEFs and whether they differed between clusters, we quantified the net abundance of our features in LADs and performed pairwise regression analysis. Whereas most correlations were weak, some significant trends were observed. As expected, we found CBX1, H3K9me3, and lamin B1 to be positively correlated with one another in all clusters (Supplemental Fig. S7A–C). The relationship between H3K9me3/CBX1 and lamin B1 was weakest in the group where they were most enriched, K9me3 LADs. Despite being depleted in both H3K9me2

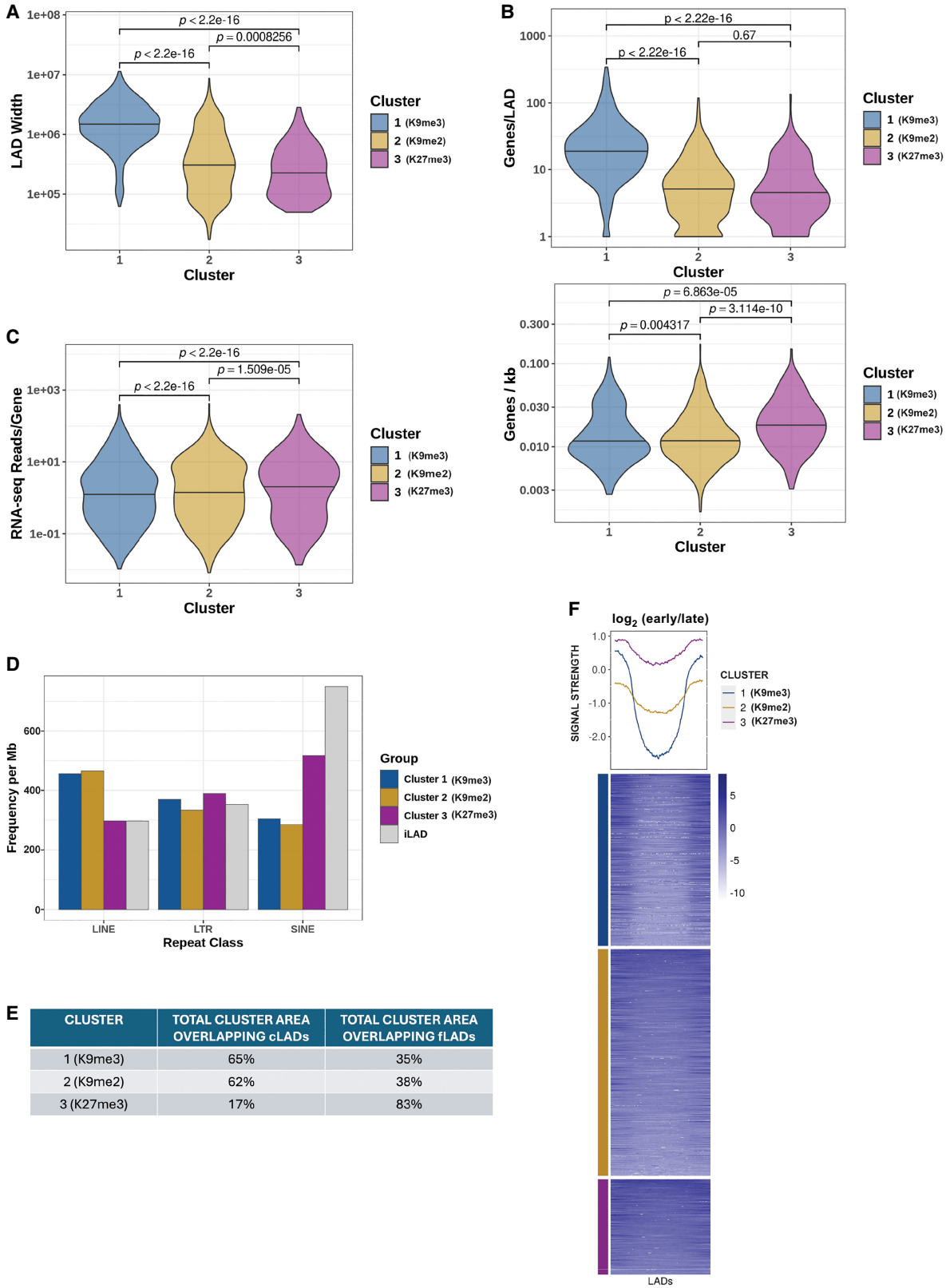

E

CLUSTER	TOTAL CLUSTER AREA OVERLAPPING cLADs	TOTAL CLUSTER AREA OVERLAPPING fLADs
1 (K9me3)	65%	35%
2 (K9me2)	62%	38%
3 (K27me3)	17%	83%

Figure 5. Comparison of K9me3 LADs, K9me2 LADs, and K27me3 LADs. (*A*) Comparison of LAD sizes (bp) between clusters. *P*-values determined by Wilcoxon rank-sum test. (*B*) Gene content in each cluster, represented by total number of genes contained in LADs from each cluster (*top*) and gene density in each cluster (*bottom*). (*C*) Gene expression from LADs of each cluster in fragments per kilobase per million (FPKM). *P*-values determined by Wilcoxon rank-sum test. (*D*) Abundance of LINE elements, SINE elements, and LTR repeats in each cluster compared to inter-LADs. (*E*) Table showing overlap between each cluster and cLADs. The cLADs set used came from a previously study which mapped LADs by DamID in several cell types (Peric-Hupkes et al. 2010). The total cLAD area overlapping our clusters does not add up to 100% because a small fraction of the LADs detected in those cells were not detected in our LAD mapping that gave rise to the clusters. (*F*) Heat map and profile of replication colored by LAD clusters. Values represent $\log_2$ early/late signal, so low values indicate late replication timing and higher values represent earlier replication timing.

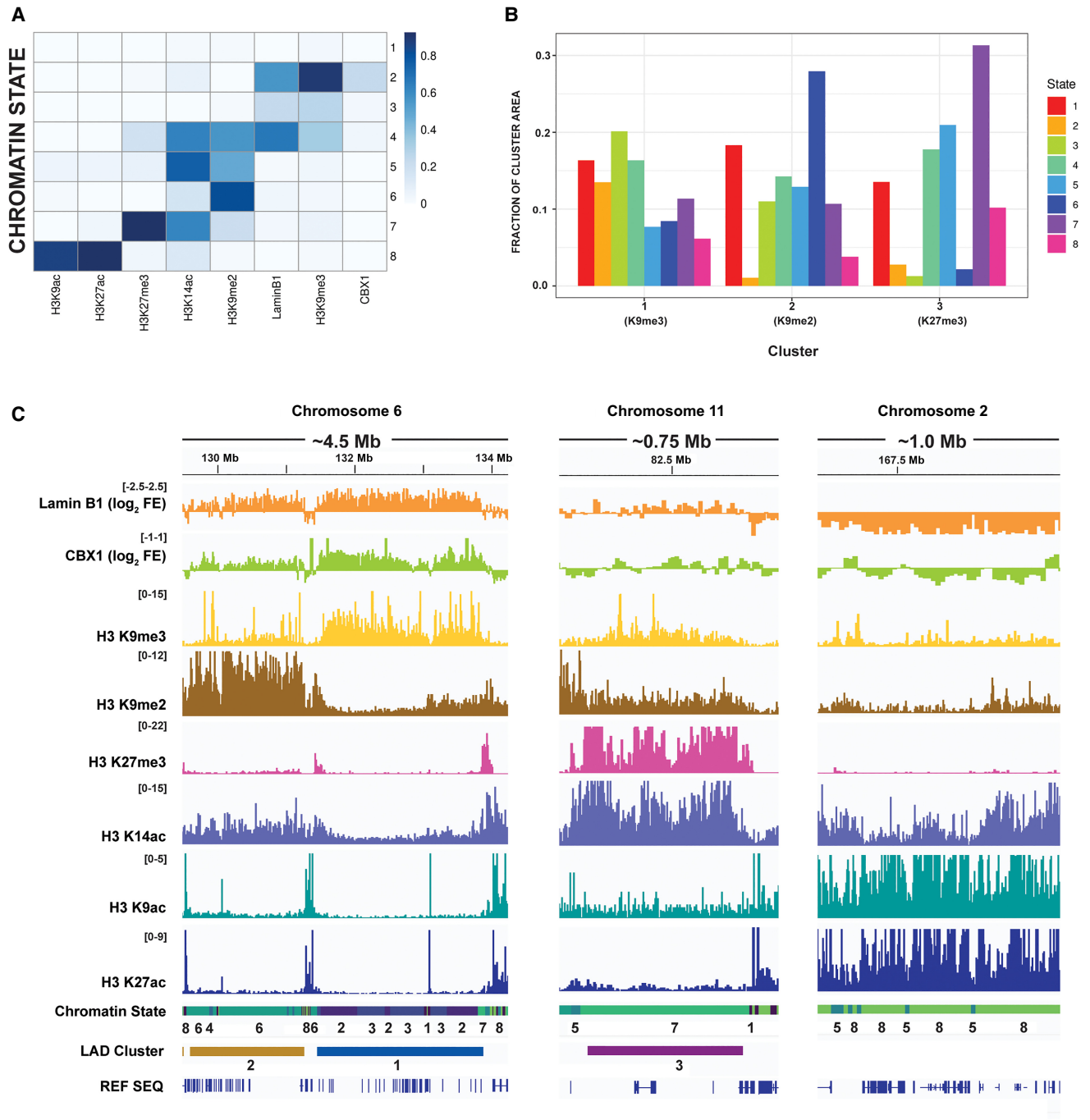

Figure 6. ChromHMM analysis and comparison with LAD clusters. (*A*) Heat map of feature probabilities in each state. Color intensity represents feature abundance in that state. ChromHMM was run with eight states using 10-kb bins. (*B*) Relative abundance of each state in Cluster 1 (K9me3 LADs), Cluster 2 (K9me2 LADs), and Cluster 3 (K27me3 LADs). Height of bars represents the fraction of 10-kb bins within that LAD cluster that correspond to that state. (*C*) IGV browser view showing example LADs from each cluster as well as a representative inter-LAD region, with the distribution of ChromHMM states across each (e.g., enrichment of states 4–6 in K9me2 LADs, states 1–3 in K9me3 LADs, and state 7 in K27me3 LADs).

and H3K27me3, K9me3 LADs also displayed a positive correlation between both of these marks and lamin B1 (Supplemental Fig. S7D,E).

Similarly, lamin B1 increased with the abundance of H3K9me3 and H3K27me3 in K9me2 LADs but showed no correlation with H3K9me2 (Supplemental Fig. S7C–E). K27me3 LADs showed no correlation between H3K27me3 and lamin B1 and only weak correlation between H3K9me2 and lamin B1 (Supplemental Fig. S7D,E). H3K14ac generally correlated with other features in a similar manner to H3K27me3, consistent with their similar patterns of enrichment across LAD clusters (Figs. 3C, 6A; Supplemental Fig. S7F,G). Notably, PTMs that correlated positively

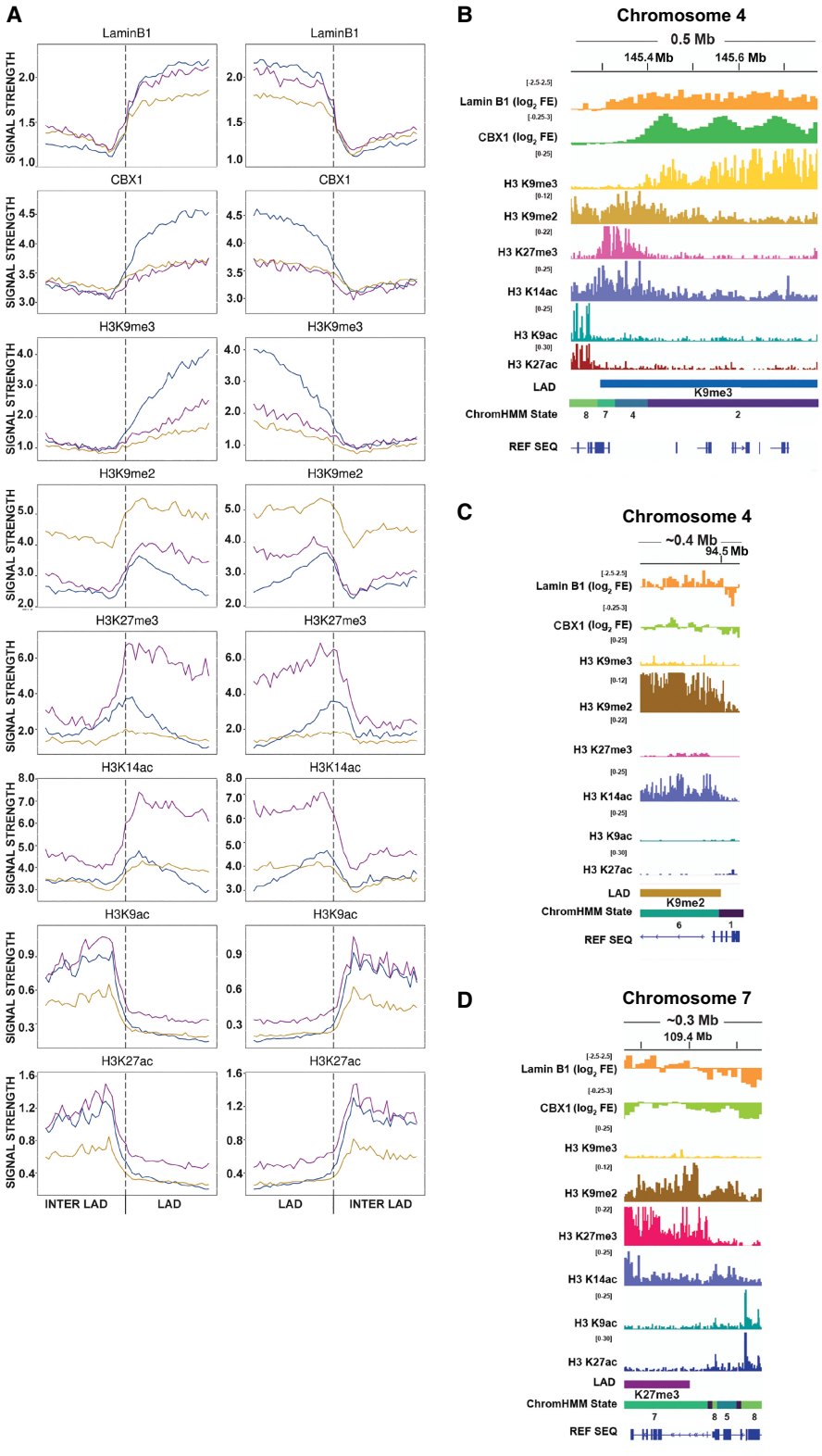

Figure 7. LAD border profiles vary between clusters. (*A*) Profiles of all features around LAD borders, with each cluster shown separately. *Y*-axis values represent signal intensity. Boxes show a 500-kb window centered around the LAD borders (vertical dotted line). For LADs that are shorter than the 250-kb range shown, the excess area beyond the opposite LAD border was not included to ensure only LAD chromatin was plotted in the area denoted as the LAD interior. (*B*) IGV browser example of epigenetic features and ChromHMM state transitions across a Cluster 1 LAD (K9me3 LAD) boundary. (*C*) IGV browser example of epigenetic features and ChromHMM state transitions across a Cluster 2 LAD (K9me2 LAD) boundary. (*D*) IGV browser example of epigenetic features and ChromHMM state transitions across a Cluster 3 LAD (K27me3 LAD) boundary.

with lamin B1 did not necessarily correlate with CBX1 and vice-versa, suggesting that some chromatin–lamina interactions are not mediated by CBX1.

Discussion

Prior studies have pointed to structural and functional differences within LADs (Bian et al. 2013; Lund et al. 2015; Zheng et al. 2015; van Steensel and Belmont 2017; Kaczmarczyk et al. 2022; Alagna et al. 2023; Shah et al. 2023; Gholamalamdari et al. 2025). Our analysis of LADs clustered by lamin B1, CBX1, H3K9me3, H3K9me2, H3K27me3, H3K14ac, H3K9ac, and H3K14ac demonstrated that LADs in MEFs fall into three distinct subtypes with significant differences in their epigenomic and genomic content. Each of the three clusters we identified has a prominent marker of heterochromatin. Cluster 1 is characterized by high levels of H3K9me3 (and is therefore referred to as K9me3 LADs), Cluster 2 has high levels of H3K9me2 (called K9me2 LADs), and Cluster 3 contains high levels of H3K27me3 (called K27me3 LADs). This study has the advantage of having mapped these features in cell lines derived from the same colony of C57BL6/J mice, avoiding possible discrepancies that could arise when using public data sets generated by different labs in their own MEF cell lines. Our approach of scaling LADs to a uniform size and dividing them into bins prior to *k*-means clustering provides the advantages of weighting all LADs equally regardless of size and allowing different patterns of the same mark across LADs to be distinguished.

K9me3 LADs and K9me2 LADs most resemble the classical definition of LADs: large, gene-poor, and enriched in LINE elements and methylation of H3K9. However, few LADs were enriched in both H3K9me2 and H3K9me3. This suggests that H3K9me2 and H3K9me3 rarely coincide significantly in LADs in iMEFs; perhaps because they are mutually exclusive on the same histone. In fact, regression analysis showed a significant negative correlation between the levels of H3K9me2 and H3K9me3 in K9me2 LADs and K9me3 LADs (Supplemental Fig. S7H). We hypothesize that H3K9 methylation is maintained primarily by SUV39H1/2 in the former and EHMT1/2 in the latter, as these primarily catalyze H3K9 trimethylation and dimethylation, respectively (Rice et al. 2003; Padeken et al. 2022). This may help explain why both sets of methyltransferases are important for lamina association (Bian et al. 2013; van Steensel and Belmont 2017).

Previous studies have affirmed the existence of small LADs with facultative heterochromatin character, but these are not well studied in comparison with large, canonical LADs (Tran et al. 2021; Alagna et al. 2023; Gholamalamdari et al. 2025). Although H3K27me3 has been proposed to play a role in attaching chromatin to the nuclear periphery, it is generally thought to be restricted to LAD borders, perhaps because LADs are often studied as a single, uniform group. By clustering LADs, we uncovered a group of LADs enriched in H3K27me3 across the entire LAD body. These LADs are smaller and more enriched in genes and SINE elements than LADs from other clusters. Approximately one-fifth of LADs in iMEFs fall in this category, but due to their small size, they compose only a small fraction of the total lamina-associated genome (6.8% as opposed to 27.9% for K9me2 LADs and 65.3% for K9me3 LADs), which may explain why they are not apparent when characterizing total LAD chromatin. One study has indicated that these LADs are more variable and interact with the nuclear periphery for only part of the cell cycle, which is consistent with their facultative heterochromatin character (Tran et al. 2021). This is consistent with our finding that a much larger fraction of K27me3 LADs varied between our LAD set and a previously published DamID LAD set than was the case for K9me2 or K9me3 LADs (Supplemental Fig. S1A).

Notably, a recent study in human cells supported LAD divisions similar to ours, noting four different LAD clusters which were H3K9me3-enriched, H3K27me3-enriched, H3K9me2-enriched, and PTM-depleted, respectively (Gholamalamdari et al. 2025). This study had clustered LADs based on their degree of association with the nuclear lamina and with nuclear speckles, thereby suggesting that these epigenetically distinct groups of LADs are subject to different regulatory mechanisms and behaviors across the cell cycle and development.

Our DNA FISH data showed differences in lamina association between clusters, with greater peripheral localization in K9me3 and K9me2 LADs than K27me3 LADs. This is consistent with the relatively high overlap between K27me3 LADs and fLADs, which contact the nuclear lamina less frequently across cell populations than cLADs (Kind et al. 2015). The cluster localization measured by DNA FISH data differs from the inferences of lamin B1 CUT&RUN signal (Fig. 3C), illustrating the need for direct 3D measurements like FISH to address such questions.

Previous studies have emphasized the importance of H3K9me2 in lamina association (Poleshko et al. 2017, 2019; Shah et al. 2023). Our results indicate that H3K9me3 and H3K27me3 are similarly important, likely pointing to the cell type–specific differences in chromatin–lamina tethering mechanisms. The relative expression levels of different lamins and lamin-associated proteins change across development and vary between tissues. H3K9me2 is neither necessary nor sufficient for association of chromatin with the nuclear periphery in all cell types (Towbin et al. 2012; Bian et al. 2013; Eberhart et al. 2013; Harr et al. 2015; Smith et al. 2021b). H3K9me3 levels correlate positively with changes in lamina association in mesenchymal cell lineages (including fibroblasts) and negatively in others (Das et al. 2023). One study examining the roles of H3K27me3, H3K9me2, and H3K9me3 in chromatin–lamina tethering in MEFs concluded that all three are required for proper chromatin–lamina interactions (Harr et al. 2015). Another found that H3K9me2 and H3K9me3 are both enriched at the nuclear periphery in MEFs but are anticorrelated, suggesting that they mark different regions governed by different peripheral targeting mechanisms (Bian et al. 2013). It is, therefore, possible that differential expression or post-translational modification of lamins or other proteins involved in mediating chromatin–lamina interactions cause different histone PTM-dependent mechanisms to predominate in different cell types (Solovei et al. 2013; Smith et al. 2021a).

Numerous mechanisms help establish and maintain borders between euchromatin and heterochromatin (Cuddapah et al. 2009; Wang et al. 2014, 2015). This is underscored by our observations of the complexity and uniqueness of LAD borders, which are particularly consequential sites for LAD regulation (Briand and Collas 2020; Alagna et al. 2023). Besides the well-characterized enrichment of H3K27me3, previous studies have identified enrichment of factors such as CTCF, macro-H2A, and gene promoters in the vicinity of LAD borders (Guelen et al. 2008; Fu et al. 2015; Harr et al. 2015; van Schaik et al. 2022). We have now identified a new feature of LAD borders, H3K14ac. H3K14ac is generally associated with transcriptional activation and has received relatively little attention compared to many other acetylation marks (Wang et al. 2008; Karmodiya et al. 2012; Regadas et al. 2021). Previous studies have shown that it is a crucial regulator of heterochromatin maintenance in fission yeast, marks a subset of

promoters and enhancers in higher eukaryotes, and is essential for mammalian development (Kueh et al. 2011, 2023; Reddy et al. 2011; Karmodiya et al. 2012; Stirpe et al. 2021; Seman et al. 2023). We find that H3K14ac accumulates just inside LAD borders and gradually decreases into the middle of the LAD, unlike H3K9ac or H3K27ac, which are highly depleted across LADs and enriched outside LADs. This suggests a role for H3K14ac in regulating LAD borders. Many LADs (most K9me2 LADs and K27me3 LADs) show moderate to high enrichment of H3K14ac across the entire LAD body as well as the borders.

We also found a moderate enrichment of H3K9me2 inside LAD borders, particularly in K9me3 LADs, which were otherwise depleted in H3K9me2. H3K9me2 has generally been seen across LAD bodies, pointing to another potential difference between cell types and LAD clusters. Notably, H3K14ac and H3K9me2 at LAD borders do not align with the well-characterized peaks of H3K27me3 at LAD borders and are instead shifted inward. The reason for this is unclear but may suggest that these marks reinforce the border by forming a second barrier against the euchromatin outside LADs.

The results of this study contribute to a growing understanding of the internal distinctions between LADs and reveal significant features shaping these differences and contributing to LAD function and regulation. They also highlight how LAD regulation may differ across different cell types, underscoring the complexity with which chromatin–lamina interactions and the mechanisms governing them are coordinated and adjusted through development and differentiation.

Methods

Cell culture

Mouse embryonic fibroblasts harvested and immortalized as previously described were cultured at 37°C with 5% CO_2 (Nagarajan et al. 2013). Cells were grown in Dulbecco's Modified Eagle's high glucose medium supplemented with 10% FBS, 1% glutamine, and 1% Pen-Strep, and passaged approximately every 2–3 days. Cells were harvested for experiments using 0.5% trypsin and resuspended in fresh media for counting.

CUT&Tag

CUT&Tag was performed according to the EpiCypher CUTANA Direct-to-PCR CUT&Tag protocol using 100,000 cells (details in Supplemental Methods), with a light crosslinking step adapted from a published protocol (Kaya-Okur et al. 2020). All CUT&Tag experiments were performed in triplicate using three independently derived cell lines from the same mouse colony.

CUT&RUN

CUT&RUN was performed according to the EpiCypher CUT&RUN protocol using 500,000 cells (details in Supplemental Methods), and libraries were prepared using the CUTANA CUT&RUN Library Prep kit. Lamin B1 CUT&RUN was performed in duplicate. CUT&RUN for H3K9me2 and H3K14ac to validate CUT&Tag results was performed in single replicate, and a nuclei extraction step was inserted prior to bead binding.

ChIP-seq and RNA-seq

CBX1 ChIP-seq was performed in biological duplicate as previously described for H3K9me2 and H3K9me3 (Popova et al. 2021). RNA-seq was performed in biological triplicate as previously described (Nagarajan et al. 2019).

Data preprocessing and LAD calling

Before alignment, raw CUT&RUN data were trimmed using Trim Galore! (https://www.bioinformatics.babraham.ac.uk/projects/trim_galore/) with the arguments -q 20 --stringency 3 --trim-n. CUT&Tag and CUT&RUN data were aligned to the mm10 genome using Bowtie 2 (Langmead and Salzberg 2012) with parameters --end-to-end --very-sensitive --no-unal --no-mixed --no-discordant --phred33 -I 10 -X 700. The mm10 build was chosen for this study because some experiments were carried out prior to the release of mm39, and, given the scale and number of the features and regions investigated, realigning to a more recent reference genome would be highly unlikely to affect results. CBX1 ChIP-seq data was aligned to the mm10 and hg19 genomes using BWA-MEM with flag -M (Li and Durbin 2009). Data was filtered to remove reads mapping to mitochondrial DNA or unlocalized or unplaced contigs. Individual replicates were merged and converted to bedGraph or bigWig format for viewing on the Integrative Genomics Viewer (IGV) (Robinson et al. 2011) and for downstream analysis.

For LAD calling, lamin B1 and IgG CUT&RUN data were normalized to the same library size using the SAMtools (Li et al. 2009) view, filtered to remove reads overlapping the ENCODE ChIP-seq blacklist, and replicates were merged. LADs were called using the HMMt package in R (https://github.com/jianhong/HMMtBroadPeak/) with a modified version of the HMMtBroadPeak function which used a sliding window to smooth the data by averaging a bin's signal with the two adjacent bins. LADs were first called by the modified function using 30-kb bins. The ends of the LADs were then adjusted to increase the resolution by running the normal HMMtBroadPeak function with 5-kb bins and using the output to trim or extend LAD ends depending on whether the overlapping 5-kb bin was LAD-positive (Supplemental Code S1).

Data clustering

For clustering, histone PTM, CBX1, and lamin B1 BED files were filtered to remove reads overlapping the ENCODE ChIP-seq blacklist and converted to bigWig format. We used deepTools computeMatrix (Ramírez et al. 2016) to scale all LADs to a size of 1 Mb and summarize bigWig signal into 50-kb bins across the LAD, including 100 kb outside the LAD border. The data was read into R (version 4.1.0) (R Core Team 2024) and filtered to remove Chr X and Chr Y, which had suboptimal LAD mapping and were excluded from analysis. Each column was then scaled to a mean of 0 and standard deviation of 1, and the data were clustered using the *k*-means function in R. The silhouette score was calculated to determine the optimal number of clusters. Hierarchical clustering was performed using the hclust function in R (https://www.rdocumentation.org/packages/stats/versions/3.6.2/topics/hclust) with the Ward D2 linkeage. To learn which marks defined the differences between clusters, we used the randomForest package (https://CRAN.R-project.org/package=randomForest) and ran the algorithm on the entire data set because our intention was simply to train the model on our data, not make predictions.

Profiles and heat maps of the resulting clusters were created with ggplot2 (Wickham 2016) and pheatmap (https://cran.r-project.org/web/packages/pheatmap/index.html) using a matrix generated in the same way as the one used for clustering but with 10-kb bins for better resolution and with 300 kb included beyond each LAD border. To prevent them from skewing the scaling of profiles and heat maps and rendering the rest of the data invisible,

strong outliers were removed from the plotting matrix by going through each column of the matrix and removing all values more than 3× the interdecile range away from the median. Code for LAD clustering and plotting can be found in Supplemental Code S2.

ChromHMM

ChromHMM 1.24 was run on BAM files for lamin B1, CBX1, H3K9me3, H3K9me2, H3K27me3, H3K14ac, H3K9ac, and H3K27ac. We used a 10-kb bin size for binarizing BAM files, then ran LearnModel with eight states and a 10-kb bin size, specifying the mm10 genome. The dense BED file was used for further analysis after first filtering to remove all bins which overlapped gaps of unknown nucleotides more than 5 kb long.

Cluster analysis

Data analysis and visualization were performed in R. Gene annotations for the RNA-seq and to calculate gene enrichment in each cluster came from GENCODE vM25. RNA-seq data was analyzed using the nf-core RNA-seq pipeline version 3.13.2 (https://nf-co.re/), and the number of reads per gene was quantified with Salmon (Patro et al. 2017). Quantified read counts were loaded into R and normalized by fragments per kilobase per million (FPKM) before plotting. The matrix to create the profile and heat map of replication timing was created by generating matrices of the repli-seq signal from early and late S-phase using deepTools, as with the other profiles and heat maps, then calculating the $\log_2$ of the early replication signal divided by the late replication signal for each bin. Repeat locations were obtained from RepeatMasker (Smit et al. 2013–2015) through the UCSC Table Browser and used to calculate their abundance in each cluster, normalized to cluster area. Gene Ontology enrichment analysis (Supplemental Code S3) was carried out using the gprofiler2 package (Kolberg et al. 2020). Tissue enrichment analysis was carried out using the TissueEnrich package (Jain and Tuteja 2019).

Box plots, bar plots, and Venn diagrams were made with ggplot2, and *P*-values for the box plots were calculated by a Wilcoxon rank-sum test using the ggsignif package. Heat maps were made with the pheatmap package.

Linear regression

To perform linear regression, the total CUT&Tag/CUT&RUN/ChIP-seq signal for the mark of interest in each LAD was summed up using BEDTools (Quinlan and Hall 2010). These values were loaded into R, filtered to remove LADs in sex chromosomes, and divided by LAD size to get the average abundance across the LAD. The data were $\log_2$-transformed to achieve a more normal distribution. Regression was performed using the linear model function in base R, and the *P*-value of the slope was reported on each plot (Supplemental Code S4).

DNA FISH

We chose three K9me3 LADs, four K9me2 LADs, and three K27me3 LADs to target with DNA FISH probes (labeled with fluorophores ATTO467N, ATTO565, and Alexa Fluor 488, respectively). LADs were selected from three different chromosomes, with a representative of every cluster chosen from each chromosome (Supplemental Table 1). Fluorescently labeled DNA FISH probe sets were custom designed and synthesized by Daicel Arbor Biosciences. For immunofluorescence/DNA FISH experiments, cells were grown on coverslips to 70%–80% confluency, fixed with 4% PFA for 10 min, and permeabilized with 0.5% Triton X-100 for 10 min. Cells were blocked in 2% BSA for 1 h at RT and incubated in primary antibody (ab133256, 1:100 in 1% BSA/PBS-T) for 3 h at RT, followed by Alexa Fluor 405–conjugated secondary antibody (ab175652, 1:500 in 1% BSA/PBS-T) for 1 h at RT. Cells were postfixed in 2% PFA followed by 0.7% Triton X-100 for 10 min each, rinsed briefly in 2× SSCT (0.1% Tween-20 in 2× saline sodium citrate), and incubated overnight in 2× SSCT/50% (v/v) formamide at 37°C. Next, coverslips were placed on 20 µL hybridization mix (2× SSCT, 50% formamide, 10% dextran sulfate, 0.4 µg/µL RNase A) with 30 pmol DNA FISH probe (10 pmol of each cluster), sealed with rubber glue, incubated at 80°C for 10 min, and transferred to 37°C overnight. Coverslips were rinsed in 2× SSCT for 30 min at 37°C, and 10 min at RT, washed briefly with PBS, and mounted on slides with Vectashield Antifade Mounting Media. Slides were left to cure at RT for >4 h, then stored at −20°C. DNA FISH was performed in biological triplicate on the same cell lines used for CUT&Tag.

DNA FISH image capture and analysis

IF/DNA FISH slides were imaged on a Zeiss LSM 900 confocal microscope. Images were taken as Z-stacks 0.18 µm apart and underwent Airyscan 3D processing (processing strength 9.0) in Zen. Image analysis, quantification, and creation of animations were carried out in Imaris (v 10.2). We analyzed 18–21 nuclei from each biological replicate, for a total of 58 nuclei. A surface object was created for Lamin A/C signal using the surfaces tool with machine learning, and spots objects were created for DNA FISH foci with dimensions of $0.4 \times 0.4 \times 1.1$ ($X \times Y \times Z$). Any spots which fell outside and did not touch the nucleus were removed from analysis. The shortest distance between focus centers and the lamina surface was then quantified, and the data from the three biological replicates were pooled and plotted in R. Negative values indicate that the center of the focus fell within the nuclear lamina surface object.

Data sources

Gene annotations for GRCm38.p6 were downloaded in GTF format from GENCODE release M25 (https://www.gencodegenes.org/mouse/release_M25.html), and chromosomes were renamed to UCSC format for consistency with the rest of our analysis.

Repli-seq data came from 4D Nucleome (data files 4DNFI9LSI1RE and 4DNFID3GEVFS) (Rivera-Mulia et al. 2018).

Repetitive Element Annotations were obtained from RepeatMasker through the UCSC Table Browser.

DamID maps of LADs and cLADs in MEFs came from the NCBI Gene Expression Omnibus (GEO; https://www.ncbi.nim.nih.gov/geo/) accession number GSE17051, and coordinates were converted from the mm9 to mm10 genome using UCSC liftOver (Peric-Hupkes et al. 2010; Meuleman et al. 2013).

Primary antibodies

CBX1: 8676 (Cell Signaling)
H3K9me3: ab8898 (abcam)
H3K9me2: ab1220 (abcam) for CUT&Tag and main analysis
H3K9me2: 39041 (Active Motif) for CUT&RUN validation
H3K27me3: 9733 (Cell Signaling)
H3K14ac: ab52946 (abcam) for CUT&Tag and main analysis
H3K14ac: MA5-32814 (Thermo Fisher) for CUT&RUN validation
H3K27ac: 8173 (Cell Signaling)
H3K9ac: 9649 (Cell Signaling)
Lamin B1: ab16048 (abcam)
Lamin A/C: ab133256 (abcam)
IgG: 13-0042 (Epicypher)

Data access

All raw and processed sequencing data generated in this study have been submitted to the NCBI Gene Expression Omnibus (GEO; https://www.ncbi.nlm.nih.gov/geo/) under accession numbers GSE281928 (CUT&RUN), GSE281927 (CUT&Tag), GSE281926 (ChIP-seq), and GSE281925 (RNA-seq).

Competing interest statement

The authors declare no competing interests.

Acknowledgments

We thank Dr. Michael Freitas for many helpful discussions. This work was supported by grant R01 GM144601 from the National Institutes of Health (National Institute of General Medical Sciences). Access to the Zeiss Confocal Microscope was provided by the OSU Department of Neuroscience and supported by grant S10 OD026842. Access to Imaris was provided by the OSU Campus Microscopy and Imaging Facility (RRID:SCR_025078) and the OSU Comprehensive Cancer Center Microscopy Shared Resource, supported in part by grant P30 CA016058 from the National Cancer Institute.

Author contributions: C.J.M. carried out CUT&Tag, CUT&RUN, DNA FISH, data analysis, and writing. P.N. generated immortalized MEF cell lines. E.A.O. performed CUT&RUN for lamin B1. L.V.P. and B.D.S. performed ChIP-seq for CBX1. M.R.P. prepared figures and supervised research. M.R.P. and B.Z.S. advised the project.

References

Ahanger SH, Delgado RN, Gil E, Cole MA, Zhao J, Hong SJ, Kriegstein AR, Nowakowski TJ, Pollen AA, Lim DA. 2021. Distinct nuclear compartment-associated genome architecture in the developing mammalian brain. *Nat Neurosci* **24:** 1235–1242. doi:10.1038/s41593-021-00879-5

Alagna NS, Thomas TI, Wilson KL, Reddy KL. 2023. Choreography of lamina-associated domains: structure meets dynamics. *FEBS Lett* **597:** 2806–2822. doi:10.1002/1873-3468.14771

Allshire RC, Madhani HD. 2018. Ten principles of heterochromatin formation and function. *Nat Rev Mol Cell Biol* **19:** 229–244. doi:10.1038/nrm.2017.119

Atlasi Y, Stunnenberg HG. 2017. The interplay of epigenetic marks during stem cell differentiation and development. *Nat Rev Genet* **18:** 643–658. doi:10.1038/nrg.2017.57

Bannister AJ, Zegerman P, Partridge JF, Miska EA, Thomas JO, Allshire RC, Kouzarides T. 2001. Selective recognition of methylated lysine 9 on histone H3 by the HP1 chromo domain. *Nature* **410:** 120–124. doi:10.1038/35065138

Bian Q, Khanna N, Alvikas J, Belmont AS. 2013. beta-Globin *cis*-elements determine differential nuclear targeting through epigenetic modifications. *J Cell Biol* **203:** 767–783. doi:10.1083/jcb.201305027

Borsos M, Perricone SM, Schauer T, Pontabry J, de Luca KL, de Vries SS, Ruiz-Morales ER, Torres-Padilla ME, Kind J. 2019. Genome–lamina interactions are established de novo in the early mouse embryo. *Nature* **569:** 729–733. doi:10.1038/s41586-019-1233-0

Briand N, Collas P. 2020. Lamina-associated domains: peripheral matters and internal affairs. *Genome Biol* **21:** 85. doi:10.1186/s13059-020-02003-5

Cuddapah S, Jothi R, Schones DE, Roh TY, Cui K, Zhao K. 2009. Global analysis of the insulator binding protein CTCF in chromatin barrier regions reveals demarcation of active and repressive domains. *Genome Res* **19:** 24–32. doi:10.1101/gr.082800.108

Das P, San Martin R, McCord RP. 2023. Differential contributions of nuclear lamina association and genome compartmentalization to gene regulation. *Nucleus* **14:** 2197693. doi:10.1080/19491034.2023.2197693

Eberhart A, Feodorova Y, Song C, Wanner G, Kiseleva E, Furukawa T, Kimura H, Schotta G, Leonhardt H, Joffe B, et al. 2013. Epigenetics of eu- and heterochromatin in inverted and conventional nuclei from mouse retina. *Chromosome Res* **21:** 535–554. doi:10.1007/s10577-013-9375-7

Escobar TM, Loyola A, Reinberg D. 2021. Parental nucleosome segregation and the inheritance of cellular identity. *Nat Rev Genet* **22:** 379–392. doi:10.1038/s41576-020-00312-w

Falk M, Feodorova Y, Naumova N, Imakaev M, Lajoie BR, Leonhardt H, Joffe B, Dekker J, Fudenberg G, Solovei I, et al. 2019. Publisher correction: Heterochromatin drives compartmentalization of inverted and conventional nuclei. *Nature* **572:** E22. doi:10.1038/s41586-019-1454-2

Fu Y, Lv P, Yan G, Fan H, Cheng L, Zhang F, Dang Y, Wu H, Wen B. 2015. Macroh2a1 associates with nuclear lamina and maintains chromatin architecture in mouse liver cells. *Sci Rep* **5:** 17186. doi:10.1038/srep17186

Gholamalamdari O, van Schaik T, Wang Y, Kumar P, Zhang L, Zhang Y, Gonzalez GAH, Vouzas AE, Zhao PA, Gilbert DM, et al. 2025. Major nuclear locales define nuclear genome organization and function beyond A and B compartments. *eLife* **13:** RP99116. doi:10.7554/eLife.99116.4

Grewal SIS. 2023. The molecular basis of heterochromatin assembly and epigenetic inheritance. *Mol Cell* **83:** 1767–1785. doi:10.1016/j.molcel.2023.04.020

Guelen L, Pagie L, Brasset E, Meuleman W, Faza MB, Talhout W, Eussen BH, de Klein A, Wessels L, de Laat W, et al. 2008. Domain organization of human chromosomes revealed by mapping of nuclear lamina interactions. *Nature* **453:** 948–951. doi:10.1038/nature06947

Guerreiro I, Kind J. 2019. Spatial chromatin organization and gene regulation at the nuclear lamina. *Curr Opin Genet Dev* **55:** 19–25. doi:10.1016/j.gde.2019.04.008

Harr JC, Luperchio TR, Wong X, Cohen E, Wheelan SJ, Reddy KL. 2015. Directed targeting of chromatin to the nuclear lamina is mediated by chromatin state and A-type lamins. *J Cell Biol* **208:** 33–52. doi:10.1083/jcb.201405110

Jain A, Tuteja G. 2019. TissueEnrich: tissue-specific gene enrichment analysis. *Bioinformatics* **35:** 1966–1967. doi:10.1093/bioinformatics/bty890

Janssen SM, Lorincz MC. 2022. Interplay between chromatin marks in development and disease. *Nat Rev Genet* **23:** 137–153. doi:10.1038/s41576-021-00416-x

Jiang L, Huang L, Jiang W. 2024. H3K27me3-mediated epigenetic regulation in pluripotency maintenance and lineage differentiation. *Cell Insight* **3:** 100180. doi:10.1016/j.cellin.2024.100180

Kaczmarczyk LS, Levi N, Segal T, Salmon-Divon M, Gerlitz G. 2022. CTCF supports preferentially short lamina-associated domains. *Chromosome Res* **30:** 123–136. doi:10.1007/s10577-022-09686-5

Karmodiya K, Krebs AR, Oulad-Abdelghani M, Kimura H, Tora L. 2012. H3k9 and H3K14 acetylation co-occur at many gene regulatory elements, while H3K14ac marks a subset of inactive inducible promoters in mouse embryonic stem cells. *BMC Genomics* **13:** 424. doi:10.1186/1471-2164-13-424

Kaya-Okur HS, Janssens DH, Henikoff JG, Ahmad K, Henikoff S. 2020. Efficient low-cost chromatin profiling with CUT&Tag. *Nat Protoc* **15:** 3264–3283. doi:10.1038/s41596-020-0373-x

Keenan CR, Coughlan HD, Iannarella N, Tapia Del Fierro A, Keniry A, Johanson TM, Chan WF, Garnham AL, Whitehead LW, Blewitt ME, et al. 2024. Suv39h-catalyzed H3K9me3 is critical for euchromatic genome organization and the maintenance of gene transcription. *Genome Res* **34:** 556–571. doi:10.1101/gr.279119.124

Kim JJ, Kingston RE. 2022. Context-specific Polycomb mechanisms in development. *Nat Rev Genet* **23:** 680–695. doi:10.1038/s41576-022-00499-0

Kind J, Pagie L, Ortabozkoyun H, Boyle S, de Vries SS, Janssen H, Amendola M, Nolen LD, Bickmore WA, van Steensel B. 2013. Single-cell dynamics of genome-nuclear lamina interactions. *Cell* **153:** 178–192. doi:10.1016/j.cell.2013.02.028

Kind J, Pagie L, de Vries SS, Nahidiazar L, Dey SS, Bienko M, Zhan Y, Lajoie B, de Graaf CA, Amendola M, et al. 2015. Genome-wide maps of nuclear lamina interactions in single human cells. *Cell* **163:** 134–147. doi:10.1016/j.cell.2015.08.040

Kiseleva AA, Cheng YC, Smith CL, Katz RA, Poleshko A. 2023. PRR14 organizes H3K9me3-modified heterochromatin at the nuclear lamina. *Nucleus* **14:** 2165602. doi:10.1080/19491034.2023.2165602

Kolberg L, Raudvere U, Kuzmin I, Vilo J, Peterson H. 2020. gprofiler2 -- an R package for gene list functional enrichment analysis and namespace conversion toolset g:Profiler. *F1000Res* **9:** 709. doi:10.12688/f1000research.24956.2

Kueh AJ, Dixon MP, Voss AK, Thomas T. 2011. HBO1 is required for H3K14 acetylation and normal transcriptional activity during embryonic development. *Mol Cell Biol* **31:** 845–860. doi:10.1128/MCB.00159-10

Kueh AJ, Bergamasco MI, Quaglieri A, Phipson B, Li-Wai-Suen CSN, Lönnstedt IM, Hu Y, Feng ZP, Woodruff C, May RE, et al. 2023. Stem cell plasticity, acetylation of H3K14, and de novo gene activation rely on KAT7. *Cell Rep* **42:** 111980. doi:10.1016/j.celrep.2022.111980

Langmead B, Salzberg SL. 2012. Fast gapped-read alignment with Bowtie 2. *Nat Methods* **9:** 357–359. doi:10.1038/nmeth.1923

Lechner MS, Schultz DC, Negorev D, Maul GG, Rauscher FJ. 2005. The mammalian heterochromatin protein 1 binds diverse nuclear proteins

through a common motif that targets the chromoshadow domain. *Biochem Biophys Res Commun* **331:** 929–937. doi:10.1016/j.bbrc.2005.04.016

Leemans C, van der Zwalm MCH, Brueckner L, Comoglio F, van Schaik T, Pagie L, van Arensbergen J, van Steensel B. 2019. Promoter-intrinsic and local chromatin features determine gene repression in LADs. *Cell* **177:** 852–864.e14. doi:10.1016/j.cell.2019.03.009

Li H, Durbin R. 2009. Fast and accurate short read alignment with Burrows–Wheeler transform. *Bioinformatics* **25:** 1754–1760. doi:10.1093/bioinformatics/btp324

Li H, Handsaker B, Wysoker A, Fennell T, Ruan J, Homer N, Marth G, Abecasis G, Durbin R; 1000 Genome Project Data Processing Subgroup. 2009. The Sequence Alignment/Map format and SAMtools. *Bioinformatics* **25:** 2078–2079. doi:10.1093/bioinformatics/btp352

Lund EG, Duband-Goulet I, Oldenburg A, Buendia B, Collas P. 2015. Distinct features of lamin A-interacting chromatin domains mapped by ChIP-sequencing from sonicated or micrococcal nuclease-digested chromatin. *Nucleus* **6:** 30–39. doi:10.4161/19491034.2014.990855

Macrae TA, Fothergill-Robinson J, Ramalho-Santos M. 2023. Regulation, functions and transmission of bivalent chromatin during mammalian development. *Nat Rev Mol Cell Biol* **24:** 6–26. doi:10.1038/s41580-022-00518-2

Makatsori D, Kourmouli N, Polioudaki H, Shultz LD, McLean K, Theodoropoulos PA, Singh PB, Georgatos SD. 2004. The inner nuclear membrane protein lamin B receptor forms distinct microdomains and links epigenetically marked chromatin to the nuclear envelope. *J Biol Chem* **279:** 25567–25573. doi:10.1074/jbc.M313606200

Manzo SG, Dauban L, van Steensel B. 2022. Lamina-associated domains: tethers and looseners. *Curr Opin Cell Biol* **74:** 80–87. doi:10.1016/j.ceb.2022.01.004

Meuleman W, Peric-Hupkes D, Kind J, Beaudry JB, Pagie L, Kellis M, Reinders M, Wessels L, van Steensel B. 2013. Constitutive nuclear lamina–genome interactions are highly conserved and associated with A/T-rich sequence. *Genome Res* **23:** 270–280. doi:10.1101/gr.141028.112

Nagarajan P, Ge Z, Sirbu B, Doughty C, Agudelo Garcia PA, Schlederer M, Annunziato AT, Cortez D, Kenner L, Parthun MR. 2013. Histone acetyl transferase 1 is essential for mammalian development, genome stability, and the processing of newly synthesized histones H3 and H4. *PLoS Genet* **9:** e1003518. doi:10.1371/journal.pgen.1003518

Nagarajan P, Agudelo Garcia PA, Iyer CC, Popova LV, Arnold WD, Parthun MR. 2019. Early-onset aging and mitochondrial defects associated with loss of histone acetyltransferase 1 (Hat1). *Aging Cell* **18:** e12992. doi:10.1111/acel.12992

Nicetto D, Zaret KS. 2019. Role of H3K9me3 heterochromatin in cell identity establishment and maintenance. *Curr Opin Genet Dev* **55:** 1–10. doi:10.1016/j.gde.2019.04.013

Nicetto D, Donahue G, Jain T, Peng T, Sidoli S, Sheng L, Montavon T, Becker JS, Grindheim JM, Blahnik K, et al. 2019. H3K9me3-heterochromatin loss at protein-coding genes enables developmental lineage specification. *Science* **363:** 294–297. doi:10.1126/science.aau0583

Padeken J, Methot SP, Gasser SM. 2022. Establishment of H3K9-methylated heterochromatin and its functions in tissue differentiation and maintenance. *Nat Rev Mol Cell Biol* **23:** 623–640. doi:10.1038/s41580-022-00483-w

Patro R, Duggal G, Love MI, Irizarry RA, Kingsford C. 2017. Salmon provides fast and bias-aware quantification of transcript expression. *Nat Methods* **14:** 417–419. doi:10.1038/nmeth.4197

Peric-Hupkes D, Meuleman W, Pagie L, Bruggeman SW, Solovei I, Brugman W, Gräf S, Flicek P, Kerkhoven RM, van Lohuizen M, et al. 2010. Molecular maps of the reorganization of genome-nuclear lamina interactions during differentiation. *Mol Cell* **38:** 603–613. doi:10.1016/j.molcel.2010.03.016

Poleshko A, Mansfield KM, Burlingame CC, Andrake MD, Shah NR, Katz RA. 2013. The human protein PRR14 tethers heterochromatin to the nuclear lamina during interphase and mitotic exit. *Cell Rep* **5:** 292–301. doi:10.1016/j.celrep.2013.09.024

Poleshko A, Shah PP, Gupta M, Babu A, Morley MP, Manderfield LJ, Ifkovits JL, Calderon D, Aghajanian H, Sierra-Pagán JE, et al. 2017. Genome-nuclear lamina interactions regulate cardiac stem cell lineage restriction. *Cell* **171:** 573–587.e14. doi:10.1016/j.cell.2017.09.018

Poleshko A, Smith CL, Nguyen SC, Sivaramakrishnan P, Wong KG, Murray JI, Lakadamyali M, Joyce EF, Jain R, Epstein JA. 2019. H3k9me2 orchestrates inheritance of spatial positioning of peripheral heterochromatin through mitosis. *eLife* **8:** e49278. doi:10.7554/eLife.49278

Popova LV, Nagarajan P, Lovejoy CM, Sunkel BD, Gardner ML, Wang M, Freitas MA, Stanton BZ, Parthun MR. 2021. Epigenetic regulation of nuclear lamina-associated heterochromatin by HAT1 and the acetylation of newly synthesized histones. *Nucleic Acids Res* **49:** 12136–12151. doi:10.1093/nar/gkab1044

Quinlan AR, Hall IM. 2010. BEDTools: a flexible suite of utilities for comparing genomic features. *Bioinformatics* **26:** 841–842. doi:10.1093/bioinformatics/btq033

Ramírez F, Ryan DP, Grüning B, Bhardwaj V, Kilpert F, Richter AS, Heyne S, Dündar F, Manke T. 2016. deepTools2: a next generation web server for deep-sequencing data analysis. *Nucleic Acids Res* **44:** W160–W165. doi:10.1093/nar/gkw257

R Core Team. 2024. *R: a language and environment for statistical computing*. R Foundation for Statistical Computing, Vienna. https://www.R-project.org/.

Reddy BD, Wang Y, Niu L, Higuchi EC, Marguerat SB, Bähler J, Smith GR, Jia S. 2011. Elimination of a specific histone H3K14 acetyltransferase complex bypasses the RNAi pathway to regulate pericentric heterochromatin functions. *Genes Dev* **25:** 214–219. doi:10.1101/gad.1993611

Regadas I, Dahlberg O, Vaid R, Ho O, Belikov S, Dixit G, Deindl S, Wen J, Mannervik M. 2021. A unique histone 3 lysine 14 chromatin signature underlies tissue-specific gene regulation. *Mol Cell* **81:** 1766–1780.e10. doi:10.1016/j.molcel.2021.01.041

Rice JC, Briggs SD, Ueberheide B, Barber CM, Shabanowitz J, Hunt DF, Shinkai Y, Allis CD. 2003. Histone methyltransferases direct different degrees of methylation to define distinct chromatin domains. *Mol Cell* **12:** 1591–1598. doi:10.1016/S1097-2765(03)00479-9

Rivera-Mulia JC, Dimond A, Vera D, Trevilla-Garcia C, Sasaki T, Zimmerman J, Dupont C, Gribnau J, Fraser P, Gilbert DM. 2018. Allele-specific control of replication timing and genome organization during development. *Genome Res* **28:** 800–811. doi:10.1101/gr.232561.117

Robinson JT, Thorvaldsdóttir H, Winckler W, Guttman M, Lander ES, Getz G, Mesirov JP. 2011. Integrative genomics viewer. *Nat Biotechnol* **29:** 24–26. doi:10.1038/nbt.1754

Sadaie M, Salama R, Carroll T, Tomimatsu K, Chandra T, Young AR, Narita M, Pérez-Mancera PA, Bennett DC, Chong H, et al. 2013. Redistribution of the lamin B1 genomic binding profile affects rearrangement of heterochromatic domains and SAHF formation during senescence. *Genes Dev* **27:** 1800–1808. doi:10.1101/gad.217281.113

Seman M, Levashkevich A, Larkin A, Huang F, Ragunathan K. 2023. Uncoupling the distinct functions of HP1 proteins during heterochromatin establishment and maintenance. *Cell Rep* **42:** 113428. doi:10.1016/j.celrep.2023.113428

Shah PP, Keough KC, Gjoni K, Santini GT, Abdill RJ, Wickramasinghe NM, Dundes CE, Karnay A, Chen A, Salomon REA, et al. 2023. An atlas of lamina-associated chromatin across twelve human cell types reveals an intermediate chromatin subtype. *Genome Biol* **24:** 16. doi:10.1186/s13059-023-02849-5

Siegenfeld AP, Roseman SA, Roh H, Lue NZ, Wagen CC, Zhou E, Johnstone SE, Aryee MJ, Liau BB. 2022. Polycomb-lamina antagonism partitions heterochromatin at the nuclear periphery. *Nat Commun* **13:** 4199. doi:10.1038/s41467-022-31857-5

Smit A, Hubley R, Green P. 2013–2015. RepeatMasker Open-4.0. http://www.repeatmasker.org.

Smith CL, Lan Y, Jain R, Epstein JA, Poleshko A. 2021a. Global chromatin relabeling accompanies spatial inversion of chromatin in rod photoreceptors. *Sci Adv* **7:** eabj3035. doi:10.1126/sciadv.abj3035

Smith CL, Poleshko A, Epstein JA. 2021b. The nuclear periphery is a scaffold for tissue-specific enhancers. *Nucleic Acids Res* **49:** 6181–6195. doi:10.1093/nar/gkab392

Solovei I, Kreysing M, Lanctôt C, Kosem S, Peichl L, Cremer T, Guck J, Joffe B. 2009. Nuclear architecture of rod photoreceptor cells adapts to vision in mammalian evolution. *Cell* **137:** 356–368. doi:10.1016/j.cell.2009.01.052

Solovei I, Wang AS, Thanisch K, Schmidt CS, Krebs S, Zwerger M, Cohen TV, Devys D, Foisner R, Peichl L, et al. 2013. LBR and lamin A/C sequentially tether peripheral heterochromatin and inversely regulate differentiation. *Cell* **152:** 584–598. doi:10.1016/j.cell.2013.01.009

Stirpe A, Guidotti N, Northall SJ, Kilic S, Hainard A, Vadas O, Fierz B, Schalch T. 2021. SUV39 SET domains mediate crosstalk of heterochromatic histone marks. *eLife* **10:** e62682. doi:10.7554/eLife.62682

Towbin BD, González-Aguilera C, Sack R, Gaidatzis D, Kalck V, Meister P, Askjaer P, Gasser SM. 2012. Step-wise methylation of histone H3K9 positions heterochromatin at the nuclear periphery. *Cell* **150:** 934–947. doi:10.1016/j.cell.2012.06.051

Tran JR, Paulson DI, Moresco JJ, Adam SA, Yates JR, Goldman RD, Zheng Y. 2021. An APEX2 proximity ligation method for mapping interactions with the nuclear lamina. *J Cell Biol* **220:** e202002129. doi:10.1083/jcb.202002129

van Schaik T, Vos M, Peric-Hupkes D, Hn Celie P, van Steensel B. 2020. Cell cycle dynamics of lamina-associated DNA. *EMBO Rep* **21:** e50636. doi:10.15252/embr.202050636

van Schaik T, Liu NQ, Manzo SG, Peric-Hupkes D, de Wit E, van Steensel B. 2022. CTCF and cohesin promote focal detachment of DNA from the nuclear lamina. *Genome Biol* **23:** 185. doi:10.1186/s13059-022-02754-3

van Steensel B, Belmont AS. 2017. Lamina-associated domains: links with chromosome architecture, heterochromatin, and gene repression. *Cell* **169:** 780–791. doi:10.1016/j.cell.2017.04.022

Vertii A, Ou J, Yu J, Yan A, Pagès H, Liu H, Zhu LJ, Kaufman PD. 2019. Two contrasting classes of nucleolus-associated domains in mouse fibroblast heterochromatin. *Genome Res* **29:** 1235–1249. doi:10.1101/gr.247072.118

Wang Z, Zang C, Rosenfeld JA, Schones DE, Barski A, Cuddapah S, Cui K, Roh TY, Peng W, Zhang MQ, et al. 2008. Combinatorial patterns of histone acetylations and methylations in the human genome. *Nat Genet* **40:** 897–903. doi:10.1038/ng.154

Wang J, Lawry ST, Cohen AL, Jia S. 2014. Chromosome boundary elements and regulation of heterochromatin spreading. *Cell Mol Life Sci* **71:** 4841–4852. doi:10.1007/s00018-014-1725-x

Wang J, Reddy BD, Jia S. 2015. Rapid epigenetic adaptation to uncontrolled heterochromatin spreading. *eLife* **4:** e06179. doi:10.7554/eLife.06179

Wickham H. 2016. *ggplot2: elegant graphics for data analysis*. Springer-Verlag, New York. https://ggplot2.tidyverse.org.

Ye Q, Worman HJ. 1996. Interaction between an integral protein of the nuclear envelope inner membrane and human chromodomain proteins homologous to *Drosophila* HP1. *J Biol Chem* **271:** 14653–14656. doi:10.1074/jbc.271.25.14653

Ye Q, Callebaut I, Pezhman A, Courvalin JC, Worman HJ. 1997. Domain-specific interactions of human HP1-type chromodomain proteins and inner nuclear membrane protein LBR. *J Biol Chem* **272:** 14983–14989. doi:10.1074/jbc.272.23.14983

Zheng X, Kim Y, Zheng Y. 2015. Identification of lamin B–regulated chromatin regions based on chromatin landscapes. *Mol Biol Cell* **26:** 2685–2697. doi:10.1091/mbc.E15-04-0210

Zullo JM, Demarco IA, Piqué-Regi R, Gaffney DJ, Epstein CB, Spooner CJ, Luperchio TR, Bernstein BE, Pritchard JK, Reddy KL, et al. 2012. DNA sequence-dependent compartmentalization and silencing of chromatin at the nuclear lamina. *Cell* **149:** 1474–1487. doi:10.1016/j.cell.2012.04.035

Received December 20, 2024; accepted in revised form July 15, 2025.